







RESEARCH ARTICLE | JANUARY 02 2020

## Femtochemistry under scrutiny: Clocking state-resolved channels in the photodissociation of $\text{CH}_3\text{I}$ in the A-band

Special Collection: [Ultrafast molecular sciences by femtosecond photons and electrons](#)

Marta L. Murillo-Sánchez ; Jesús González-Vázquez ; María E. Corrales; Rebeca de Nalda; Emilio Martínez-Núñez ; Alberto García-Vela ; Luis Bañares  



*J. Chem. Phys.* 152, 014304 (2020)

<https://doi.org/10.1063/1.5134473>



View  
Online



Export  
Citation

[CrossMark](#)

# Femtochemistry under scrutiny: Clocking state-resolved channels in the photodissociation of CH<sub>3</sub>I in the A-band

Cite as: J. Chem. Phys. 152, 014304 (2020); doi: 10.1063/1.5134473

Submitted: 30 October 2019 • Accepted: 9 December 2019 •

Published Online: 2 January 2020



Marta L. Murillo-Sánchez,<sup>1</sup> Jesús González-Vázquez,<sup>2</sup> María E. Corrales,<sup>1</sup> Rebeca de Nalda,<sup>3</sup> Emilio Martínez-Núñez,<sup>4</sup> Alberto García-Vela,<sup>5</sup> and Luis Bañares<sup>1,6,a)</sup>

## AFFILIATIONS

<sup>1</sup>Departamento de Química Física, Facultad de Ciencias Químicas (Unidad Asociada de I+D+i al Consejo Superior de Investigaciones Científicas), Universidad Complutense de Madrid, 28040 Madrid, Spain

<sup>2</sup>Departamento de Química and Institute for Advanced Research in Chemical Sciences (IAdChem), Módulo 13, Facultad de Ciencias, Universidad Autónoma de Madrid, 28049 Madrid, Spain

<sup>3</sup>Instituto de Química Física Rocasolano, CSIC, C/ Serrano 119, 28006 Madrid, Spain

<sup>4</sup>Departamento de Química Física, Universidade de Santiago de Compostela, 15782 Santiago de Compostela, Spain

<sup>5</sup>Instituto de Física Fundamental, CSIC, C/ Serrano 123, 28006 Madrid, Spain

<sup>6</sup>Instituto Madrileño de Estudios Avanzados en Nanociencia (IMDEA-Nanoscience), Cantoblanco, 28049 Madrid, Spain

**Note:** This paper is part of the JCP Special Topic on Ultrafast Molecular Sciences by Femtosecond Photons and Electrons.

**a) Author to whom correspondence should be addressed:** [lbanares@ucm.es](mailto:lbanares@ucm.es)

## ABSTRACT

Clocking of electronically and vibrationally state-resolved channels of the fast photodissociation of CH<sub>3</sub>I in the A-band is re-examined in a combined experimental and theoretical study. Experimentally, a femtosecond pump-probe scheme is employed in the modality of resonant probing by resonance enhanced multiphoton ionization (REMPI) of the methyl fragment in different vibrational states and detection through fragment velocity map ion (VMI) imaging as a function of the time delay. We revisit excitation to the center of the A-band at 268 nm and report new results for excitation to the blue of the band center at 243 nm. Theoretically, two approaches have been employed to shed light into the observations: first, a reduced dimensionality 4D nonadiabatic wavepacket calculation using the potential energy surfaces by Xie *et al.* [J. Phys. Chem. A **104**, 1009 (2000)]; and second, a full dimension 9D trajectory surface-hopping calculation on the same potential energy surfaces, including the quantization of vibrational states of the methyl product. In addition, high level *ab initio* electronic structure calculations have been carried out to describe the CH<sub>3</sub> 3p<sub>z</sub> Rydberg state involved in the (2 + 1) REMPI probing process, as a function of the carbon-iodine (C–I) distance. A general qualitative agreement is obtained between experiment and theory, but the effect of methyl vibrational excitation in the umbrella mode on the clocking times is not well reproduced. The theoretical results reveal that no significant effect on the state-resolved appearance times is exerted by the nonadiabatic crossing through the conical intersection present in the first absorption band. The vibrationally state resolved clocking times observed experimentally can be rationalized when the (2 + 1) REMPI probing process is considered. None of the other probing methods applied thus far, i.e., multiphoton ionization photoelectron spectroscopy, soft X-ray inner-shell photoelectron spectroscopy, VUV single-photon ionization, and XUV core-to-valence transient absorption spectroscopy, have been able to provide quantum state-resolved (vibrational) clocking times. More experiments would be needed to disentangle the fine details in the clocking times and dissociation dynamics arising from the detection of specific quantum-states of the molecular fragments.

Published under license by AIP Publishing. <https://doi.org/10.1063/1.5134473>

## I. INTRODUCTION

The idea of timing chemical reactions, in the sense of measuring the time lapses necessary for chemical rearrangement to occur, has been central to Femtochemistry since its early days in the late 1980s, when Zewail saw the possibility to directly watch the elementary bond cleavage in a molecule using the new capabilities offered by subpicosecond and later femtosecond lasers<sup>1–3</sup> and applied it for the first time to monitor the C–I bond cleavage of the ICN molecule in real time.<sup>4</sup>

The participation of resonant and nonresonant signals and how these are a function of the bandwidth and temporal duration of the pulse used for probing a fast reaction were already the subject of Zewail's seminal papers.<sup>2–5</sup> For the so-called clocking experiments, light pulses that are resonant with the given electronic transitions of the products of the reaction are employed, either through one photon or multiphoton radiative or nonradiative transitions where the observable may be either light (in laser-induced fluorescence experiments)<sup>4</sup> or ionized fragments [in resonance enhanced multiphoton ionization (REMPI) experiments].<sup>6</sup> In any case, the appearance of a detectable signal indicates that the optical detection window of products is open and the delay for this to happen is a measurement of the reaction time.<sup>1–3</sup>

The A-band of CH<sub>3</sub>I has been one of the prototype systems for ultrafast studies, since dissociation in this band is direct and occurs in the femtosecond regime upon absorption. The reduced number of atoms of the molecule, and in contrast, the richness of phenomena involved in dissociation, makes it a particularly attractive system. Spectroscopically, the A-band is a structureless absorption continuum in the ultraviolet region (220–350 nm), with a maximum at about 260 nm.<sup>7</sup> It corresponds to an  $n \rightarrow \sigma^*$  transition where a non-bonding  $p$  electron of iodine is promoted to the lowest energy available antibonding molecular orbital. The heavy iodine atom causes strong spin-orbit coupling, and as a result, the electronic configuration contains five states, named  $^3Q_2$ ,  $^3Q_1$ ,  $^3Q_0+$ ,  $^3Q_0-$ , and  $^1Q_1$  in Mulliken notation, all of which are strongly repulsive along the C–I coordinate. Three of these are accessible through dipole allowed transitions: two weak perpendicular transitions to the  $^3Q_1$  and  $^1Q_1$  states and a strong parallel transition to the  $^3Q_0+$  state (thus, the  $^3Q_0+$  state will be subsequently called  $^3Q_0$ ). In fact, in the maximum of the absorption band, absorption of light takes place almost exclusively upon excitation through a strong parallel transition from the ground electronic state to the  $^3Q_0$  electronic state. Excitation of this surface adiabatically leads to the formation of the iodine atom in its spin-orbit excited state,  $I^*(^2P_{1/2})$ , whereas all the other surfaces correlate with ground state iodine atoms,  $I(^2P_{3/2})$ . The presence of nonadiabatic couplings between the surfaces—the most relevant of which is the conical intersection between the  $^3Q_0$  and the  $^1Q_1$  states—complicates the origin of iodine atoms, which can, in principle, be produced via both adiabatically and nonadiabatically. In a first approximation, it is possible to conceive this process as an essentially one-dimensional problem, given the lightness of the hydrogen atoms attached to the carbon atom, and the fact that dissociation is direct and fast along the C–I bond. However, some of the other degrees of freedom play an essential role in the process, in aspects as fundamental as the nonadiabatic crossing that leads to the formation of iodine atoms, which is only possible when the  $C_{3v}$  symmetry is broken<sup>8</sup> (which corresponds to H<sub>3</sub>C–I bending during dissociation). It

is also important to recall that the CH<sub>3</sub> moiety changes from pyramidal to planar geometry, which causes important umbrella mode excitation.

Extensive experimental work has been devoted to the study of this fundamental process, both in asymptotic (using nanosecond pulsed lasers)<sup>9–13</sup> and time-resolved (using femtosecond pulsed lasers) contributions.<sup>14–19</sup> Eppink and Parker applied their newly discovered velocity map imaging technique to the study of this process<sup>10,11</sup> across the full A-band, while the blue<sup>12</sup> and red<sup>13</sup> edges of the absorption band have been explored with slice imaging and nanosecond pulsed lasers.

Also, numerous theoretical works have dealt with this problem,<sup>8,15,16,20–28</sup> using various approaches including a full-dimensional (9D) quantum dynamics study.<sup>27</sup> Despite the intense efforts, controversy or discrepancy with experiment persists on aspects such as the description of the absorption spectrum, the relevance of the absorption strength to the three dipole-allowed  $^3Q_1$ ,  $^1Q_1$ , and  $^3Q_0$  states, or the CH<sub>3</sub>-vibrationally selected quantum yields.

The comparison of wavepacket calculations performed for the center of the A-band in CH<sub>3</sub>I with the results of femtosecond velocity map imaging experiments was reported a few years ago.<sup>15,16</sup> The CH<sub>3</sub>I photodissociation dynamics was studied using a wavepacket model including four degrees (4D) of freedom,<sup>16</sup> namely, the C–I dissociation coordinate, the I–CH<sub>3</sub> bending mode, the CH<sub>3</sub> umbrella mode, and the C–H symmetric stretch mode. The theoretical reaction times were compared with those obtained in femtosecond velocity map imaging experiments. The model reproduced very well the experimental reaction times for the CH<sub>3</sub>( $v_1$ ,  $v_2$ ) +  $I^*(^2P_{1/2})$  dissociation channels with  $v_1 = 0$  and  $v_2 = 0, 1, 2$  and also for the channel CH<sub>3</sub>( $v_1 = 0$ ,  $v_2 = 0$ ) +  $I(^2P_{3/2})$ . The model failed, however, to predict the experimental clocking times for the CH<sub>3</sub>( $v_1$ ,  $v_2$ ) +  $I(^2P_{3/2})$  channels with ( $v_1$ ,  $v_2$ ) = (0, 1), (0, 2), and (1, 0), i.e., when the CH<sub>3</sub> fragment produced along with spin-orbit ground state I atoms is vibrationally excited. Different explanations were given for the disagreement, but the differences have not been assessed definitely.

Meanwhile, experiments on the photodissociation of CH<sub>3</sub>I in the A-band using different spectroscopic techniques for probing the fragments in a time-resolved fashion and even following the time evolution of the transition-state region have been carried out in the last few years.<sup>29–33</sup> Attar *et al.*<sup>29</sup> were the first to measure the transition-state region in the A-band photodissociation of CH<sub>3</sub>I at 266 nm using femtosecond extreme ultraviolet (XUV) transient absorption spectroscopy by real-time evolution of core-to-valence transitions near the iodine N-edge at 45–60 eV. Core-to-valence electronic states decay during the C–I bond cleavage simultaneously to the  $I(^2P_{3/2})$  and  $I^*(^2P_{1/2})$  fragment resonant appearance. They found that the transition-state resonances reach a maximum at ~40 fs and decay to complete C–I dissociation in ~90 fs. Later, Drescher *et al.*<sup>30</sup> reported similar experiments as those of Ref. 29, but they observed a continuous shift in energy of the emerging atomic absorption lines that were attributed to relaxation of the valence shell vacancy that occurs during the first few femtoseconds of the C–I bond dissociation.

Baumann *et al.*<sup>31</sup> performed single-shot UV/VUV pump-probe experiments to study the valence state photodissociation of CH<sub>3</sub>I

after excitation at 268 nm and probing by one- or two-photon ionization at 161 nm with a sub-10 fs time resolution. The reversed order of the UV and VUV femtosecond laser pulses allowed them to study the dissociation from the  $6p$  ( $^2E_{3/2}$ ) Rydberg state after excitation at 161 nm and probing by multiphoton ionization at 268 nm. They attributed time constants of  $98.2 \pm 1.9$  fs and  $28.5 \pm 2.8$  fs for the biexponential decay of the  $\text{CH}_3\text{I}$  parent ion of the  $3Q_0$  and  $^1Q_1$  states, respectively. The  $^3Q_0$  time constant was directly related to the C–I bond cleavage along the reaction coordinate up to the asymptotic region of the potential energy surface, whereas the  $^1Q_1$  time constant was attributed to the duration of the  $^1Q_1 \rightarrow \tilde{X}^1E_{3/2}$  ionization window considering the restrictions imposed by the VUV probing wavelength (161 nm). Mechanisms were proposed to account for the time constants observed for the fragment ions  $\text{I}^+$  and  $\text{CH}_3^+$ .<sup>31</sup>

Inner-shell photoelectron spectroscopy was employed by Brauße *et al.*<sup>32</sup> to time-resolve the ultrafast photodissociation of  $\text{CH}_3\text{I}$  at 272 nm in the form of structural and electronic transformations, using  $\sim 120$  fs soft-X-ray pulses centered at 11.6 nm as a probe, to ionize above the iodine  $4d$  edge, and photoelectron-photoion coincidences. The observed reduction in the intensity of the iodine  $4d$  peak in the photoelectron spectrum together with the appearance of a contribution attributed to the ionization of iodine atoms was assigned to the evolution from the bound molecule to the isolated fragment atom, although the time resolution of the experiment was not enough to fully resolve the process.

Finally, Warne *et al.*<sup>33</sup> studied the time-resolved pump-probe photodissociation of  $\text{CH}_3\text{I}$  on the red (269 nm) and blue (255 nm) parts around the center of the A-band by UV (395 nm) multiphoton ionization photoelectron spectroscopy. Surprisingly, they observed different dynamics at the two excitation wavelengths with significant differences in the measured reaction times and dynamic structure, which were attributed to a significant contribution of the  $^1Q_1$  state at the excitation wavelength of 255 nm, i.e., a more complex structure in the photoelectron spectrum and increased appearance time, indicative of a more complex reaction pathway on the  $^1Q_1$  potential energy surface.

In this work, we present a combined experimental and theoretical study where excitation slightly to the red (268 nm) and to the blue (243 nm) of the A-band of  $\text{CH}_3\text{I}$  (maximum at 260 nm) is explored in detail, providing new insights into the unresolved issues concerning the quantum state (vibrational and electronic) resolved clocking times for this photodissociation process. It is, to the best of our knowledge, the first time where time-resolved measurements are carried out nearer to the blue edge of the band, which is of particular interest due to the possible contribution of more than one excited state.<sup>13</sup> Furthermore, improvements in the analysis of the velocity map images as a function of time delay has permitted a more detailed determination of anisotropies in the spatial distribution of the methyl fragments and reaction (clocking) times. The findings are rationalized with the help of two combined theoretical approaches, a 4D wavepacket calculation and a full dimension (9D) trajectory surface hopping calculation with quantization of the final vibrational states of the methyl fragment, which help in unraveling the complex dynamics at play in the fast photodissociation of this prototypical polyatomic molecule.

## II. METHODOLOGIES

### A. Experimental

The femtosecond laser system, a chirped pulse amplified Ti:sapphire, delivers 3.5 mJ pulses of 50 fs duration at a repetition rate of 1 kHz with a tunable central wavelength of about 804 nm. The output of the amplifier is split in two arms to provide the pump and probe pulses.

In the pump arm, UV femtosecond laser pulses are produced for the excitation of  $\text{CH}_3\text{I}$  in its first absorption band (A-band). For this purpose, the fundamental output ( $\sim 1$  mJ) is used to pump a two-stage femtosecond automated optical parametric amplifier (TOPAS). The output signal is then twice frequency doubled in two  $\beta$ -barium borate (BBO) crystals in order to obtain tunable radiation at the blue side of the A-band, at 243 nm, with  $7\text{--}9$   $\mu\text{J}$ /pulse. Alternatively, for excitation at the center of the A-band at 268 nm, the fundamental output is frequency tripled with BBO crystals.

The probe arm is designed to provide radiation to resonantly ionize the  $\text{CH}_3$  products by  $(2 + 1)$  REMPI through the  $3p_z$  Rydberg state. The fundamental beam is used to pump an optical parametric amplifier (OPA), where signal and idler pulses are generated in a BBO crystal. The signal pulse is later frequency quadrupled to constitute the probe beam providing tunable pulses in the 325–334 nm region with pulse energies typically around  $6\text{--}7$   $\mu\text{J}$  and with a full width at half maximum (FWHM) bandwidth of  $\approx 3$  nm. Tuning these pulses in the above-mentioned range allows  $(2 + 1)$  REMPI detection of  $\text{CH}_3$  radicals in different vibrational states: vibrationless state  $v = 0$  at 333.5 nm, symmetric stretch excited  $v_1 = 1$  at 333.9 nm, umbrella-mode excited  $v_2 = 1$  and  $v_2 = 2$  at 329.4 nm and 325.8 nm, respectively, and accidentally the corresponding combination bands  $(v_1, v_2) = (1, 1)$  and  $(v_1, v_2) = (1, 2)$ .

The linear polarization of the pump and probe laser beams is set up horizontal by means of half-wave plates and the propagation conditions are controlled through adjustable telescopes. The pump and probe beams are propagated collinearly and finally focused with a 25 cm focal length lens into a vacuum chamber where they interact with a pulsed molecular beam.

The supersonic molecular beam is generated by expansion of  $\text{CH}_3\text{I}$  at  $0^\circ\text{C}$  in helium at a backing pressure of 1.5–2 bars, through a 0.5 mm diameter nozzle, 1 kHz homemade cantilever piezoelectric pulsed valve.<sup>15</sup> A 1 mm diameter skimmer separates the expansion and ionization chambers, where the molecular beam interacts with the laser pulses. Clustering conditions in the beam are avoided by maintaining low enough pressure and working on the initial part of the molecular beam pulse.

The delay between the pump and probe pulses is controlled by a motorized delay stage placed at the probe laser arm that allows time steps as low as 1 fs. The instrument temporal response time, considered as the temporal cross correlation of the pump and probe pulses, is measured through multiphoton ionization of Xe, obtaining typical values of 150 fs.

After interaction with the laser pulses, the formed ions are extracted in the vertical direction by a set of electrostatic lenses working in the velocity mapping configuration;<sup>34</sup> typical repeller voltages are 5200 V, with optimum velocity mapping conditions found for  $V_{\text{extractor}}/V_{\text{repeller}} = 0.76$ . The field-free time-of-flight (TOF) region is 50 cm long. The detector is composed of a dual

microchannel plate (MCP) in the Chevron configuration, coupled to a phosphor screen. Mass selection is achieved through gating the gain in the front MCP plate. The images thus generated on the phosphor screen are recorded with a Peltier-cooled 12 bit charge-coupled device camera.

The energy calibration of the apparatus is done by measuring the  $\text{CH}_3^+$  image upon 268 nm photodissociation of  $\text{CH}_3\text{I}$  and resonant multiphoton ionization of  $\text{CH}_3(\nu = 0)$  and using the known kinetic energy release (KER) of the  $\text{CH}_3(\nu = 0) + \text{I}^*(^2P_{1/2})$  and  $\text{CH}_3(\nu = 0) + \text{I}(^2P_{3/2})$  channels.<sup>11,15</sup>

For the realization of a clocking experiment, once the signal is optimized and the time overlap is found, several sets of images are acquired as the pump-probe delay is scanned over a given time range. Each image is the result of accumulating over 800 laser shots. Finally, the equivalent images of all the sets are added together. Images are Abel inverted using the polar basis set expansion (pBasex) method,<sup>35</sup> and a multidimensional fitting model is used for the analysis of the data.<sup>36</sup> This model will be described in some detail below.

For the clocking measurements, two different methods have been employed for the determination of time zero, i.e., the temporal overlap between the pump and probe lasers. First, typical *in situ* measurements of the transient from multiphoton ionization of xenon were performed, allowing the pump-probe cross-correlation function (120 fs) to be also measured. Second, a low-energy contribution appearing in the centre of all images, which is attributed to multiphoton dissociative ionization processes, has also been used. Both transients are fitted to Gaussian functions, and they coincide with each other within  $\pm 20$  fs.

## B. 4D wavepacket calculations

The  $\text{CH}_3\text{I}$  molecule is an ideal prototype to develop theoretical models to describe photodissociation processes.<sup>37,38</sup> In this work, the  $\text{CH}_3\text{I}$  system is represented by considering four degrees of freedom ( $R, r, \alpha, \theta$ ), where the dissociation coordinate  $R$  is the distance between I and the  $\text{CH}_3$  center-of-mass,  $r$  is the symmetric C–H bond distance representing the  $\text{CH}_3$  symmetric stretch mode ( $\nu_1$  mode),  $\alpha$  is the umbrella bending angle of the  $\text{CH}_3$  group ( $\nu_2$  mode), and  $\theta$  is the in-plane  $\text{H}_3\text{–C–I}$  bending angle ( $\nu_6$  mode) between the C–I axis and the axis perpendicular to the plane containing the three hydrogen atoms.<sup>16</sup> Wavepacket simulations including five degrees of freedom, namely, the current four modes plus the out-of-plane bending mode, have shown that this latter mode plays a small role in the  $\text{CH}_3\text{I}$  photodissociation dynamics and can be ignored,<sup>23</sup> and this is why it is neglected in the present model. Furthermore, full-dimensional, 9D calculations carried out using the multiconfiguration time-dependent Hartree (MCTDH) scheme have been reported,<sup>27</sup> and they show that the 5D and 9D descriptions lead to rather similar results. Thus, it is expected that the four modes considered in the current model are able to reliably describe the main features of the  $\text{CH}_3\text{I}$  nonadiabatic photodissociation dynamics in the A-band. It is also noted that the present model allows one to represent the dynamics of the  $\text{CH}_3$  symmetric stretch mode  $\nu_1$  and to describe dissociation channels producing  $\text{CH}_3$  fragments in the  $\nu_1 = 0$  and 1 states, which are probed experimentally.

At the  $\lambda = 243$  and 268 nm excitation wavelengths used in this work, the intensity of the  $^3Q_1 \leftarrow \tilde{X}^1A_1$  transition is very small, as shown by the experimental data and the theoretical A-band spectrum.<sup>12</sup> Thus, in the present model, the  $^3Q_1 \leftarrow \tilde{X}^1A_1$  transition is neglected and only the  $^3Q_0 \leftarrow \tilde{X}^1A_1$  and  $^1Q_1 \leftarrow \tilde{X}^1A_1$  transitions are considered. A detailed description of the representation of the potential energy surfaces of the different electronic states involved in the photodissociation process and of the transition dipole moment functions for the  $^3Q_0 \leftarrow \tilde{X}^1A_1$  and  $^1Q_1 \leftarrow \tilde{X}^1A_1$  transitions has been given elsewhere.<sup>8,12,15,16,24–26</sup> The Hamiltonian, the wavepacket method used to simulate the photodissociation of  $\text{CH}_3\text{I}$ , and the procedure applied to obtain the observable quantities of interest have been described in detail previously.<sup>16</sup>

There is, however, a significant difference between the present calculations and those of the previous work.<sup>16</sup> In the earlier work, all the calculated magnitudes were averaged over the spectral bandwidth of both the pump and probe pulses used in the experiment.<sup>16</sup> Taking into account the influence of these experimental conditions in the simulations led to a more favorable comparison between the experimental and theoretical results. As previously described,<sup>16</sup> the experimental detection energy window originated by the probe pulse bandwidth was simulated in the calculations by projecting out the wavepacket at different asymptotic  $\text{CH}_3\text{–I}$  distances,  $R_c$ , and averaging over the results obtained. Such an average over the probe pulse spectral bandwidth has been suppressed in the present simulations (albeit the average over the pump pulse bandwidth is still performed), and currently, the magnitudes of interest, and particularly the appearance times, are calculated by projecting out the wavepacket only at the single asymptotic distance  $R_c = 13$  bohrs (6.88 Å), the same one that is used in the surface-hopping trajectory simulations (see below). This asymptotic distance has been chosen considering that the interaction between the heavy iodine atom and the electronic states of the methyl fragment, especially those with Rydberg character, is negligible as reflected in the *ab initio* calculations of the Rydberg states of the methyl fragment as a function of the C–I distance (see below), and thus, the methyl fragment can be considered as a purely free fragment. Although choosing an asymptotic distance is always arbitrary, the aim here is to use similar conditions in the calculation of the observable quantities in both the wavepacket and trajectory treatments, in order to make the corresponding results as comparable as possible and not influenced by the probing process. This way we can observe subtle effects on the clocking times due to, for instance, the nonadiabatic crossing through the conical intersection between the  $^3Q_0$  and  $^1Q_1$  potential energy surfaces, the methyl vibrational mode selectivity, or the different available energies for the bond cleavage depending on the final vibrational and electronic states of the fragments.

It is well known that the transition dipole moment functions based on *ab initio* data used to describe the  $^1Q_1 \leftarrow \tilde{X}^1A_1$  transition clearly overestimates the absorption to this state in comparison with experimental determinations.<sup>12,16</sup> This is especially relevant in this work, since we have studied the photodissociation of  $\text{CH}_3\text{I}$  in the blue part of the A-band at 243 nm, where according to the theoretical absorption spectrum, the  $^1Q_1$  state will absorb substantially in an amount comparable to the absorption to the  $^3Q_0$  state<sup>12</sup> (see Fig. 1).



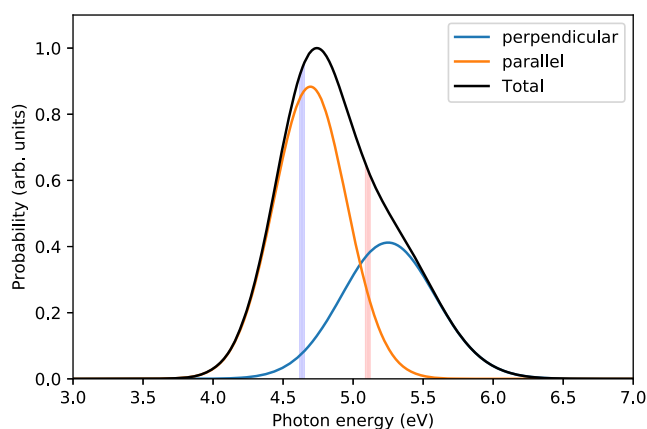


**FIG. 1.** Semiclassical absorption spectrum corresponding to the  ${}^3Q_0 \leftarrow \tilde{X}^1A_1$  (parallel) and the  ${}^1Q_1 \leftarrow \tilde{X}^1A_1$  (perpendicular) transitions calculated with  $2 \times 10^6$  initial conditions using a Wigner distribution. The vertical bars represent the selected trajectories for excitation at 243 nm (orange) and 268 nm (violet) considering the femtosecond laser pulse bandwidth. Note that the contribution from the perpendicular transition is clearly overestimated in comparison with experimental determinations<sup>7</sup> when using the transition dipole moments based on the *ab initio* data of Alekseyev *et al.*<sup>26</sup> as modeled in Ref. 12.

### C. 9D surface-hopping trajectory calculations

The laser induced nonadiabatic dynamics has been simulated in full dimensionality by using semiclassical methodology. In this methodology, the nuclear degrees of freedom follow the classical Newton equations and the electronic dynamics is described by the time-dependent Schrödinger equation. We use the SHARC method<sup>39</sup> in combination with the full dimension potential energy surfaces reported by Amatatsu *et al.*<sup>8,24</sup>

First, the minimum geometry and harmonic frequencies are obtained using perturbation theory (CASPT2) from a state average complete active space calculation including the first 3 singlet states using the 6-31G basis set and a pseudopotential for the iodine atom. The lone pairs of the iodine atom and the I–C bonding and antibonding orbitals were included in the active space SA3-CASPT2(6,4). These calculations have been performed with the MOLPRO package.<sup>40</sup>

Using this geometry, a set of  $2 \times 10^6$  initial conditions was created using a Wigner distribution that was employed to evaluate the semiclassical spectrum depicted in Fig. 1, considering both transitions to the  ${}^3Q_0$  and to the  ${}^1Q_1$  states according to the model from Ref. 12. Using this spectrum, a stochastic sampling of initial conditions was performed in the energy regions between 5.08 and 5.12 eV (for excitation at 243 nm) and between 4.61 and 4.65 eV (for excitation at 268 nm), selecting 22 850 and 74 140 initial conditions, respectively. Trajectories using these sets of initial conditions were run with the SHARC code<sup>39</sup> during 300 fs using the full dimensional (9D) analytical potential energy surfaces described by Amatatsu *et al.*<sup>8</sup> and corrected by Xie *et al.*<sup>24</sup> During each trajectory calculation, the adiabatic surfaces were obtained by the diagonalization of the electronic Hamiltonian (potential and diabatic couplings) where the gradient was evaluated to follow the classical movement. On the other hand, the dynamics of the electronic wavefunction was

followed using a Runge-Kutta algorithm of fourth order. A stochastic algorithm based on the density<sup>41</sup> was employed to decide the electronic state where the potential runs using a surface hopping algorithm.

Finally, the fragment kinetic energy and the appearance time were recorded for every trajectory. The appearance time was obtained employing the same methodology described in the wavepacket calculations, i.e., for every trajectory, the time where the distance between the I atom and the CH<sub>3</sub> moiety is 13 bohrs (6.88 Å) was recorded.

To obtain the vibrational quantum numbers of the methyl fragment, the normal mode analysis (NMA) approach of Corchado and Espinosa-García is employed.<sup>42</sup> Briefly, in the NMA method, the vibrational energy content of each vibrational mode  $i$ ,  $E_i$ , is the sum of a kinetic,  $E_{kin,i}$ , and a potential energy  $E_{pot,i}$ , which are computed from the projection onto the normal mode space of the momenta and unscaled Cartesian coordinates of the fragment, respectively. Corchado and Espinosa-García have also incorporated an anharmonic correction and Coriolis coupling to the NMA approach.<sup>42</sup> The method has been tested against the Fast Fourier Transform (FFT) method<sup>43–46</sup> for polyatomic molecules and the Einstein-Brillouin-Keller (EBK)<sup>47</sup> method for diatomics. NMA has also been recently employed to study the vibrational energy distributions of hydrogen cyanide, resulting in the photolysis of vinyl cyanide<sup>48</sup> and methyl cyanoformate.<sup>49</sup>

### D. *Ab initio* calculations of the CH<sub>3</sub> Rydberg states

In order to evaluate the influence of the proximity of the iodine atom to the energy of the CH<sub>3</sub> Rydberg states involved in the (2 + 1) REMPI probing process used in this work, the relevant Rydberg states have been calculated as a function of the C–I distance with restricted active space methods. The basis set was constructed by using a complete ANO-RCC basis set<sup>50</sup> in the CH<sub>3</sub> radical, whereas in the I atom, a triple zeta contraction scheme was employed. In this way, it is possible to describe very diffuse orbitals in the CH<sub>3</sub> radical, maintaining a reasonable computational cost. The active space was selected in the dissociating limit including the three lone pairs of the I atom together with the lone electron, and the Rydberg orbitals, 3s and 3p<sub>z</sub>, of the CH<sub>3</sub> fragment. In order to reduce the size of the configuration space, a restricted active space formalism was followed. In our case, we divide the space into two parts: the RAS2 space containing the I orbitals and the lone pair in the CH<sub>3</sub> fragment, where all excitations are allowed, and the Rydberg orbitals in the RAS3 space, where only single excitations were possible. Two state-averaged calculations were performed for 16 singlet and 15 triplet states. Relativistic effects were considered by using a Douglas-Kroll Hamiltonian,<sup>51</sup> and the spin-orbit coupling between the singlet and triplet manifolds was computed in the frame of the Atomic Mean Field Approximation (AMFI),<sup>52</sup> obtaining a total of 61 electronic states. Finally, a one dimensional grid was calculated by freezing the CH<sub>3</sub> moiety in its CASPT2 minimum and the I atom approaches starting at 10 Å until 4 Å. These calculations were performed with the OpenMolcas code.<sup>53</sup>

In order to calculate the adiabatic potential energy curves for the umbrella mode, a 2D grid including the  $R$  and  $r$  distances, representing dissociation and umbrella modes, was constructed. For every  $R$  distance, the vibrational levels in the umbrella mode

were estimated using the Fourier grid Hamiltonian method<sup>54</sup> in the  $r$  grid.

### III. RESULTS

#### A. Experimental results

The experimental observables are the  $\text{CH}_3$  fragment velocity map ion (VMI) images obtained after photodissociation of  $\text{CH}_3\text{I}$  excited at the center (268 nm) and at the blue side (243 nm) of the A-band, followed by vibrationally state resolved resonant multi-photon ionization of the  $\text{CH}_3(\nu)$  fragment in a pump-probe fashion as a function of the time delay. Since the results at 268 nm have been the subject of previous publications,<sup>14–16</sup> more emphasis will be placed here on the results at 243 nm and the comparison with respect to the center-of-the-band excitation. The first part of this section will present results concerning the formation of vibrationless methyl fragments ( $\nu = 0$ ), and the second part will describe the formation of umbrella mode excited methyl ( $\nu_2$ ).

The inverted  $\text{CH}_3(\nu = 0)$  fragment images obtained from the photodissociation of  $\text{CH}_3\text{I}$  at 243 nm and 268 nm detected via  $(2 + 1)$  REMPI at 333.5 nm ( $Q$  branch of the two-photon  $3p_z\ ^2A_2'' \leftarrow\ ^2A_2''\ 0_0^0$  transition) for an asymptotic pump-probe time delay, i.e., when the reaction can be considered as finished and the fragments enough separated at a distance implying a negligible interaction between them (resonant condition in Femtochemistry for the clocking of the reaction), are shown in Fig. 2. The weak signal in the center of the images is attributed to dissociative ionization processes, which are not the subject of this study, and thus, in the following, we shall concentrate on the higher kinetic energy rings. The corresponding center-of-mass methyl fragment translational energy distributions (TEDs) resulting from the angular integration of the inverted images are depicted in the right panels of Fig. 2. Maximum available energies expected for each channel were obtained from literature values for dissociation energy, iodine spin-orbit splitting, and  $\text{CH}_3$  vibrational quanta,<sup>10,15</sup> and upon neglecting the internal energy content of the parent molecule. They are indicated with dashed vertical lines in Fig. 2.

Nanosecond experiments with  $(2 + 1)$  REMPI  $\text{CH}_3(\nu = 0)$  detection report two channels as shown by the more intense inner and outer rings, which are assigned to the channels  $\text{CH}_3(\nu = 0) + \text{I}^*(^2P_{1/2})$  and  $\text{CH}_3(\nu = 0) + \text{I}(^2P_{3/2})$  [indicated, respectively, by (3) and (1) in Figs. 2(b) and 2(d)].<sup>10,11</sup> However, for femtosecond pulse probing, it has already been shown that a third middle ring is distinguished after excitation at 268 nm and assigned to the channel yielding  $\text{CH}_3(\nu_1 = 1) + \text{I}(^2P_{3/2})$ <sup>14,15</sup> [indicated as (2) in Figs. 2(b) and 2(d)]. This ring is detectable accidentally due to the spectral proximity of the  $1_1^1$  and  $0_0^0$  bands of  $\text{CH}_3$ , both within the bandwidth of the femtosecond probe laser.<sup>14,15</sup> Upon excitation at 243 nm, a fourth weak ring with the lowest translational energy can be observed and attributed to the channel yielding symmetric-stretch mode excited  $\text{CH}_3(\nu_1 = 1)$  in correlation with  $\text{I}^*(^2P_{1/2})$ . This new photodissociation channel, marked as (4) in Fig. 2(d), is open due to the larger amount of energy available for the fragments with this shorter excitation wavelength.

Analogous images were measured for the probe laser tuned to the  $Q$  branch of the two-photon  $3p_z\ ^2A_2'' \leftarrow\ ^2A_2''\ 2_1^1$  and  $2_2^2$  transitions for  $\text{CH}_3$ , i.e., predominantly  $(2 + 1)$  REMPI probing

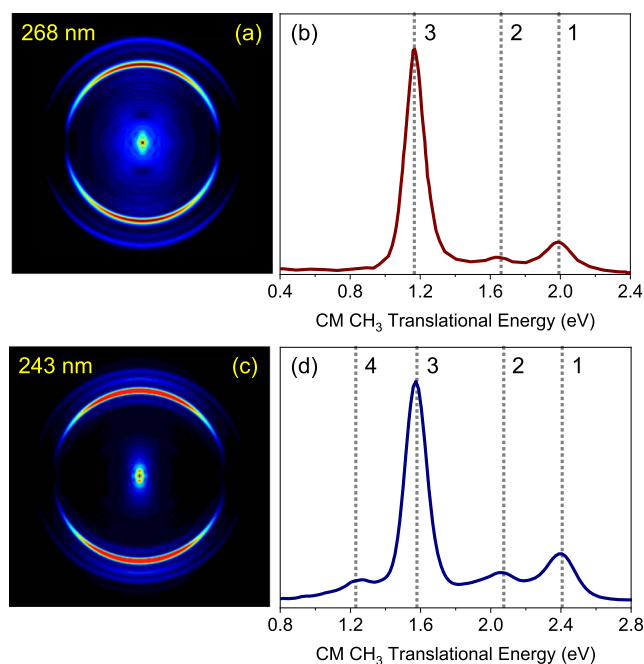


**FIG. 2.** Asymptotic Abel inverted  $\text{CH}_3$  images and the corresponding center-of-mass translational energy distribution (TED) obtained upon  $\text{CH}_3\text{I}$  excitation at [(a) and (b)] 268 nm and [(c) and (d)] 243 nm and  $\text{CH}_3$   $(2 + 1)$  REMPI detection at 333.5 nm and at 10 ps pump-probe time delay. The polarization axis of the pump and probe pulses is vertical. Contributions to the images and TEDs are indicated by dashed vertical lines and numbered according to the following assignments: (1)  $\text{CH}_3(\nu = 0) + \text{I}(^2P_{3/2})$ , (2)  $\text{CH}_3(\nu_1 = 1) + \text{I}(^2P_{3/2})$ , (3)  $\text{CH}_3(\nu = 0) + \text{I}^*(^2P_{1/2})$ , and (4)  $\text{CH}_3(\nu_1 = 1) + \text{I}^*(^2P_{1/2})$ . Detection of  $\text{CH}_3(\nu_1 = 1)$  with a  $(2 + 1)$  REMPI for the  $1_1^1$  band at 333.9 nm is accidental due to the bandwidth of the probe femtosecond laser pulse centered at 333.5 nm.

umbrella mode-excited  $\text{CH}_3(\nu_2 = 1)$  and  $\text{CH}_3(\nu_2 = 2)$ , at wavelengths 329.4 and 325.8 nm, respectively.<sup>15</sup> These images are not shown for brevity, but they are very similar to those measured for excitation at 268 nm reported in our previous work.<sup>15</sup> In the present case, for excitation at 243 nm, there appear rings associated with the channels  $\text{CH}_3(\nu_2 = 1, 2) + \text{I}(^2P_{3/2})$ ,  $\text{CH}_3(\nu_1 = 1, \nu_2 = 1, 2) + \text{I}(^2P_{3/2})$ ,  $\text{CH}_3(\nu_2 = 1, 2) + \text{I}^*(^2P_{1/2})$ , and  $\text{CH}_3(\nu_1 = 1, \nu_2 = 1, 2) + \text{I}^*(^2P_{1/2})$ .

As is clear from the images depicted in Fig. 2, the angular character of all the A-band photodissociation contributions observed is parallel (i.e., maximizing along the polarization axis of the electric field of the laser) for excitation at 268 nm and at 243 nm. The angular distributions can be obtained by radial integration of the images across each of the selected ranges for each channel. A detailed analysis of the angular distributions of the different dissociation channels has been carried out considering the possibility of polarization effects for the  $\text{CH}_3$  fragment ascribed to rotational alignment.<sup>12,13</sup> The angular distributions have been fitted to the commonly used expression for one-photon dissociation and a  $(2 + 1)$  REMPI detection process,<sup>12,13</sup>

$$I(\theta) = \frac{\sigma}{4\pi} [1 + \beta_2 P_2(\cos \theta) + \beta_4 P_4(\cos \theta) + \beta_6 P_6(\cos \theta)], \quad (1)$$

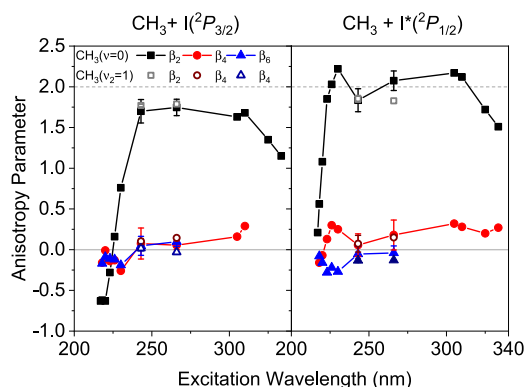


**FIG. 3.** Anisotropy parameters  $\beta_2$ ,  $\beta_4$ , and  $\beta_6$  obtained from the fit of the angular distributions extracted from the asymptotic images measured at 333.5 and 329.5 nm probing, i.e., for the detection of  $\text{CH}_3(v=0)$  (depicted in Fig. 2) and  $\text{CH}_3(v_2=1)$  (not shown). Error bars represent the standard deviation of the analysis of several measurements. The present anisotropy values obtained at excitation wavelengths 243 and 268 nm are represented together with those reported in Refs. 12 and 13 from nanosecond experiments in the red and blue edges of the absorption A-band.

where  $\theta$  is the angle between the photofragment recoil direction and the photolysis polarization direction,  $\sigma$  is the absorption cross section (since the experimental setup has not been calibrated for total intensities, the quotient has been treated as a normalization fitting parameter),  $\beta_i$  are anisotropy parameters, which reflect the dissociation dynamics and the photofragment polarization, and  $P_i$  are the Legendre polynomials of  $i$ th order. If no photofragment polarization is expected, Eq. (1) can be truncated in  $i = 2$ , and for this particular case,  $\beta_2$  coincides with the anisotropy parameter  $\beta$ .

The anisotropy parameter values obtained from the fits of the angular distributions for the dissociation channels yielding  $\text{CH}_3(v=0)$  and  $\text{CH}_3(v_2=1)$  for the excitation wavelengths 243 and 268 nm are depicted in Fig. 3 along with those obtained in nanosecond experiments in the red and blue edges of the A-band.<sup>12,13</sup> As can be seen, the  $\beta_4$  and  $\beta_6$  values returned from the fit at the two excitation wavelengths studied in this work (243 and 268 nm) are small and approximately constant, which indicates that fragment polarization effects are minor. Therefore, the photodissociation

anisotropy parameter  $\beta$  should be closely connected to the measured  $\beta_2$  parameter. The large values of  $\beta_2$ , being indeed around the limiting value of 2 allowed for a pure parallel transition, for both the  $\text{I}^*(^2P_{1/2})$  and  $\text{I}(^2P_{3/2})$  channels and for both  $\text{CH}_3$  in  $v=0$  and  $v_2=1$  vibrational states, clearly state that excitation is carried out predominantly to the  $^3Q_0$  state, and consequently, no participation of direct dissociation from the perpendicular  $^1Q_1$  state is expected at the two excitation wavelengths studied in this work. The decrease in the  $\beta_2$  values measured in the red and blue edges of the A-band<sup>12,13</sup> depicted in Fig. 3 highlight indeed the increasing participation of the perpendicular  $^3Q_1$  and  $^1Q_1$  states, respectively, when reaching the limits of excitation at 333.45 nm and 217 nm, respectively.

Methyl images detected at 333.5 nm have been recorded as a function of the pump-probe time delay for excitation to both the center and the blue side of the absorption band. The results are presented in Fig. 4 for the case of excitation at 243 nm. It is observed that at very short time delays, the dominant contribution in the images is multiphoton dissociative ionization, which appears in the center of the image, but as time delay increases, this contribution gradually decreases and eventually disappears and at the same time the intensity of the rings becomes stronger. Similar sets of time-dependent images were acquired for the probe laser wavelengths 329.4 and 325.8 nm, respectively, for the detection of  $\text{CH}_3(v_2=1)$  and  $\text{CH}_3(v_2=2)$  (not shown).

The images were angularly integrated to obtain the corresponding  $\text{CH}_3$  translational energy distributions (TEDs) for each time delay. Figure 5 shows the time-dependent TEDs in the form of 2D maps for all three probe wavelengths (333.5, 329.5, and 325.8 nm) for excitation at 243 nm.

For the analysis of the maps shown in Fig. 5, a multidimensional fitting method has been employed through parameterized functions that describe each of the contributions to the image radially, angularly, and temporally. The minimization algorithm employed to find optimum parameters is a Levenberg-Marquardt nonlinear regression method that is applied globally to the complete set of images. The method has been described previously in detail.<sup>36</sup> In this work, it has proven essential to deal with the full Abel-inverted images, and not only with the TEDs, due to overlapping contributions that could only be disentangled through the consideration of the angular coordinate.<sup>55</sup> The main values of interest to extract from such an analysis are the appearance (clocking) times of each of the channels. For this matter, resonant

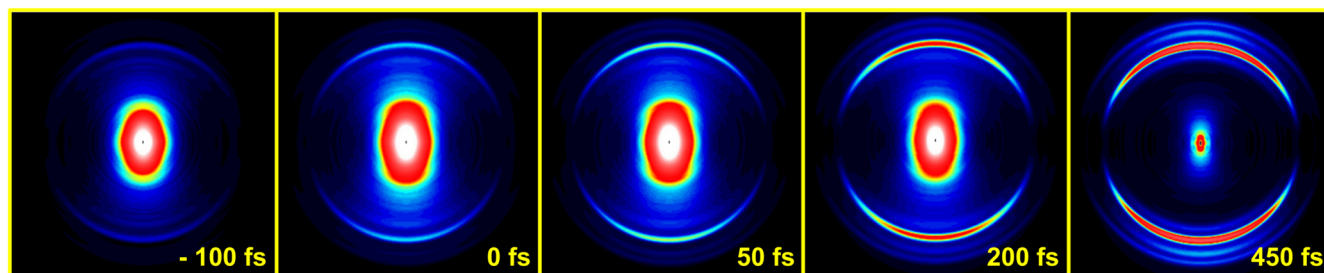


**FIG. 4.** Sequence of Abel-inverted  $\text{CH}_3$  images obtained upon  $\text{CH}_3\text{I}$  excitation at 243 nm and  $\text{CH}_3$  detection by  $(2+1)$  REMPI at 333.5 nm as a function of the indicated pump-probe time delay.



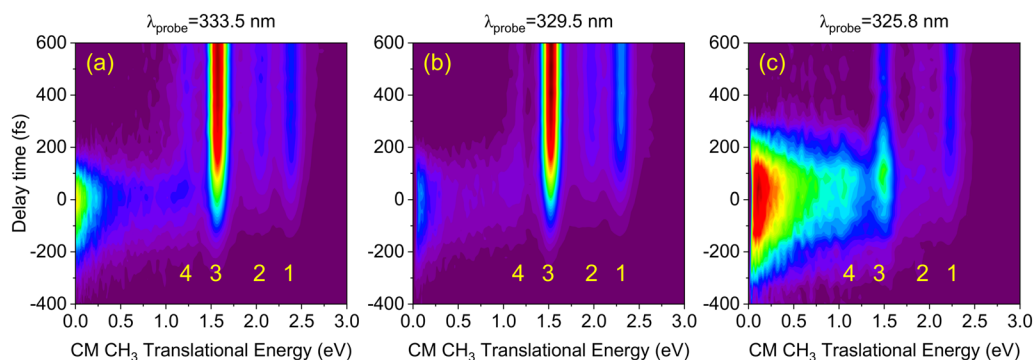


**FIG. 5.** 2D maps of the center-of-mass (CM) translational energy distributions of  $\text{CH}_3$  upon excitation of  $\text{CH}_3\text{I}$  at 243 nm as a function of time delay for (2 + 1) REMPI probing of methyl at (a) 333.5 nm, (b) 329.5 nm, and (c) 325.8 nm. The vertical peaks shown in (a) correspond to the four rings depicted in Figs. 2(c) and 4. Vibrationless  $\nu = 0$  methyl is visible, formed in correlation with ground  $\text{I}^2(\text{P}_{3/2})$  and spin-orbit excited  $\text{I}^*(\text{P}_{1/2})$  fragments (labeled 1 and 3, respectively). Methyl with one quantum in the symmetric stretch mode  $\nu_1 = 1$  is formed in correlation with ground  $\text{I}^2(\text{P}_{3/2})$  and spin-orbit excited  $\text{I}^*(\text{P}_{1/2})$  (labeled 2 and 4, respectively). In (b), the observed channels are  $\text{CH}_3(\nu_2 = 1) + \text{I}^2(\text{P}_{3/2})/\text{I}^*(\text{P}_{1/2})$  (labeled 1 and 3) and  $\text{CH}_3(\nu_1 = 1, \nu_2 = 1) + \text{I}^2(\text{P}_{3/2})/\text{I}^*(\text{P}_{1/2})$  (labeled 2 and 4), and in (c), the observed channels are  $\text{CH}_3(\nu_2 = 2) + \text{I}^2(\text{P}_{3/2})/\text{I}^*(\text{P}_{1/2})$  (labeled 1 and 3) and  $\text{CH}_3(\nu_1 = 1, \nu_2 = 2) + \text{I}^2(\text{P}_{3/2})$  (labeled 2).

contributions were temporally described with a Boltzmann sigmoidal curve of the form

$$S = A_2 + \frac{A_1 - A_2}{1 + e^{(t-t_0)/t_c}}, \quad (2)$$

which is characterized by a center temporal position  $t_0$ , i.e., the time delay for which the intensity has reached half its asymptotic value, and a rise time constant  $t_c$ . Their radial behavior was modeled with Gaussian functions, and angularly they were described as a combination of even Legendre polynomials up to fourth order.

The transients obtained for 243 nm excitation using this method are shown in Fig. 6, where the different curves correspond to the channels observed and listed in Table I. The solid lines correspond to the temporal amplitude of each component as fitted with optimized parameters according to Eq. (2). The dashed vertical lines mark the optimized value of  $t_0$  in each case. The points on the

graph are obtained as the result of integrating the global intensity of the experimental image at each delay and subtracting the sum of all other components as fitted through the global fit procedure described above. Simulation of the central part of the image, where the signal originates from multiphoton dissociative ionization processes, is shown as the first curve on the top of each panel, and its maximum is taken as the reference time or time zero. As the transients in Fig. 6 show, all measured appearance times are in the 50–145 fs range, the shortest clocking times corresponding to the measurements performed at the probe wavelength of 333.5 nm for the detection of vibrationless  $\text{CH}_3$ .

Similar measurements and analyses were performed for excitation at 268 nm, revisiting those carried out in the past in our group,<sup>15</sup> but with a better cross correlation between the pump and probe pulses, better signal-to-noise ratios, and a careful analysis of the data following the procedure indicated above based on the multidimensional fitting strategy reported in Ref. 36.

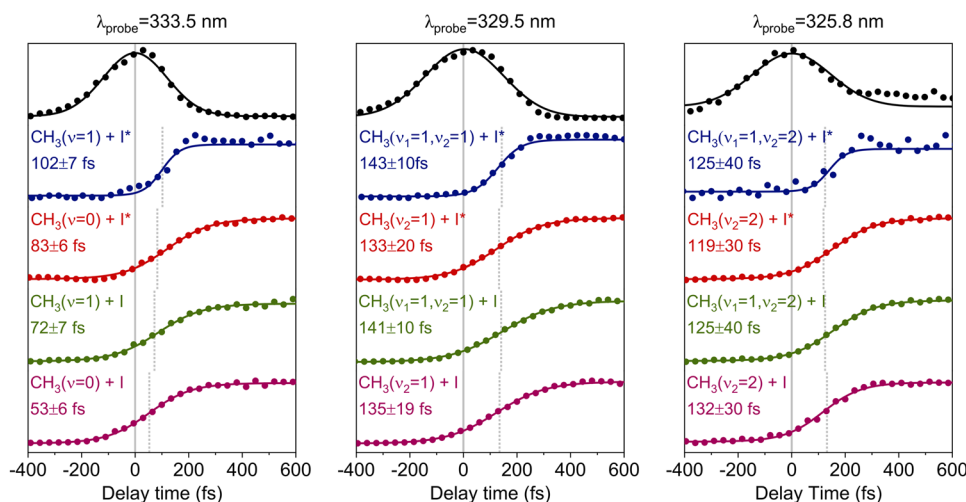


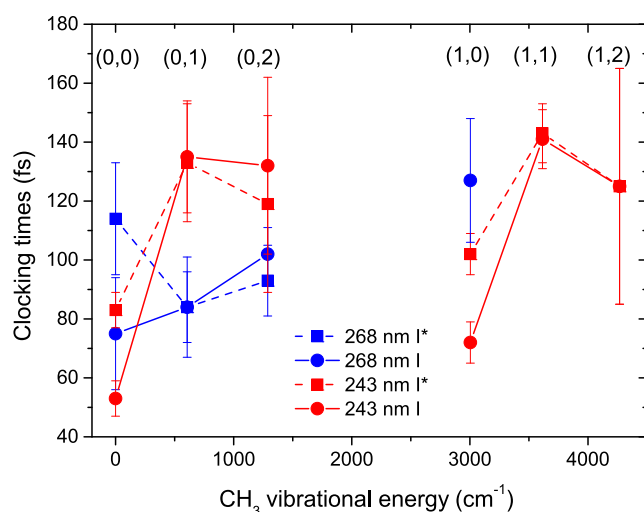
**FIG. 6.**  $\text{CH}_3$  transients corresponding to the dissociation channels indicated observed upon (2 + 1) REMPI probing at 333.5 nm, 329.5 nm, and 325.8 nm after excitation of  $\text{CH}_3\text{I}$  at 243 nm. The multiphoton dissociative ionization transients measured set the time zero for our clock, which is indicated by the solid vertical line in each plot. The dashed vertical lines in each transient represent the half of the rise of the sigmoidal signal and, therefore, give the appearance times with respect to time zero. The clocking times (with statistical uncertainties) are indicated in each transient.

**TABLE I.** Appearance (clocking) times  $\tau$  (in fs), differences between appearance times  $\Delta\tau$ , and  $I/I^*$  branching ratios measured for the different channels of the A-band photodissociation of  $\text{CH}_3\text{I}$  at the excitation wavelengths  $\lambda_{\text{exc}}$  268 nm and 243 nm. Statistical uncertainties obtained from various experiments carried out in each case are indicated.

$\text{CH}_3(\nu_1, \nu_2)$	(0, 0)	(1, 0)	(0, 1)	(1, 1)	(0, 2)	(1, 2)
$\lambda_{\text{exc}} = 268 \text{ nm}$						
$I(^2P_{3/2}), \tau \text{ (fs)}$	$75 \pm 19$	$127 \pm 21$	$84 \pm 12$	$182 \pm 10$	$102 \pm 9$	$202 \pm 3$
$I^*(^2P_{1/2}), \tau \text{ (fs)}$	$114 \pm 19$	...	$84 \pm 17$	...	$93 \pm 12$	...
$\Delta\tau \text{ (fs)}$	$34 \pm 38$	...	$0 \pm 29$	...	$-9 \pm 21$	...
$I/I^* \text{ ratio}$	0.22	...	0.33	...	1.15	...
$\lambda_{\text{exc}} = 243 \text{ nm}$						
$I(^2P_{3/2}), \tau \text{ (fs)}$	$53 \pm 6$	$72 \pm 7$	$135 \pm 19$	$141 \pm 10$	$132 \pm 30$	$125 \pm 40$
$I^*(^2P_{1/2}), \tau \text{ (fs)}$	$83 \pm 6$	$102 \pm 7$	$133 \pm 20$	$143 \pm 10$	$119 \pm 30$	$125 \pm 40$
$\Delta\tau \text{ (fs)}$	$30 \pm 12$	$30 \pm 14$	$-2 \pm 39$	$2 \pm 20$	$-13 \pm 7$	$0 \pm 80$
$I/I^* \text{ ratio}$	0.22	...	0.39	...	1.07	...

The main quantitative results obtained from the data acquired at the center of the absorption band (268 nm excitation) and the blue side of the absorption band (243 nm excitation) are summarized in Table I. In Table I, the experimental appearance (clocking) times,  $\tau$ , for all quantum (vibrational and electronic) state-resolved channels at both excitation wavelengths, the differences between clocking times,  $\Delta\tau$ , and the  $I/I^*$  ratios are presented. Figure 7 depicts the clocking times of the different state-resolved channels as a function of the vibrational energy content of the  $\text{CH}_3$  fragment.

As shown in Table I and Fig. 7, the appearance times measured for the formation of vibrationless  $\text{CH}_3(\nu = 0)$  follow the expected trend as a function of the increasing excitation energy, i.e.,

**FIG. 7.** Appearance (clocking) times (with statistical error bars) measured for the different  $\text{CH}_3(\nu_1, \nu_2) + I/I^*$  channels of the photodissociation of  $\text{CH}_3\text{I}$  at 268 nm and 243 nm as a function of the excess vibrational energy of the  $\text{CH}_3$  fragment.

a reduction of the reaction time as more energy is available to be transformed into translational energy. This is valid for the comparison between ground state  $I(^2P_{3/2})$  and spin-orbit excited state  $I^*(^2P_{1/2})$  at a given excitation energy, with systematically longer reaction times for  $I^*(^2P_{1/2})$ —about 30–35 fs, and is also valid for the comparison between the center (268 nm) and the blue side (243 nm) absorption of the A-band, with shorter times as more available energy is introduced into the system, i.e., faster dissociation after absorption in the blue side of the band.

The interpretation of the reaction times measured for vibrationally excited methyl channels (in  $\nu_1$  and  $\nu_2$  modes) is considerably more complex. The best example is the relative appearance times ( $\Delta\tau$ ) measured for  $\text{CH}_3(\nu_2 > 0)$  in correlation with ground state  $I(^2P_{3/2})$  and spin-orbit excited state  $I^*(^2P_{1/2})$ , which show a decreasing trend as vibrational excitation in  $\nu_2$  increases, being practically 0 fs for  $\text{CH}_3(\nu_2 = 1)$  and even inverting their appearance times for  $\text{CH}_3(\nu_2 = 2)$ , at both 268 nm and 243 nm excitation. Interestingly, the same trend in the relative appearance times occur for  $\text{CH}_3(\nu_1 = 1)$  as excitation in  $\nu_2$  increases, as can be inspected in the right part of Fig. 7 and in Table I.

We would like to highlight an important difference between the appearance times measured at 243 and 268 nm. Whereas  $\tau$  decreases as  $\nu_2$  excitation increases for  $\nu_1 = 0$  at 268 nm excitation, in agreement with previous observations,<sup>15</sup> the opposite trend is observed for both  $\nu_1 = 0$  and  $\nu_1 = 1$  at 243 nm excitation. Indeed,  $\tau$  increases substantially when passing from  $\text{CH}_3(\nu = 0)$  to  $\text{CH}_3(\nu_2 = 1)$  for both  $I(^2P_{3/2})$  and  $I^*(^2P_{1/2})$  channels. Considering the decrease in  $\tau$  observed at 243 nm for vibrationless  $\text{CH}_3(\nu = 0)$  in comparison with excitation at 268 nm, commented on above, umbrella-mode vibrational excitation in  $\text{CH}_3$  implies a quite substantial and unexpected increase in the clocking time at this excitation wavelength, which is absent at 268 nm excitation. Specifically, clocking times go from  $53 \pm 6$  fs to  $135 \pm 19$  fs and from  $83 \pm 6$  fs to  $133 \pm 20$  fs for the  $I(^2P_{3/2})$  and  $I^*(^2P_{1/2})$  channels, respectively, when the methyl umbrella mode is excited with one quantum.

It is interesting to note that these apparent anomalies in the clocking times appear when observation of the process is made through the umbrella mode excited components of the outgoing vibrational wavepacket. Indeed, it is this mode that shows the highest activity as dissociation proceeds, reflecting the fact that the  $\text{CH}_3$  fragment undergoes a dramatic change in its equilibrium geometry, from pyramidal to planar. Thus, as absorption to the  $\text{CH}_3\text{I}$  A-band takes place, a hot vibrational wavepacket is launched, with most of the excitation concentrated in the umbrella mode. This mode is characterized by a relatively low vibrational frequency and a correspondingly long vibration period (55 fs), which is of the order of the dissociation times. Moreover, a vibrational inversion is known to occur after the nonadiabatic transition from the  $^3Q_0$  to the  $^1Q_1$  states, which characterizes the appearance of ground state  $\text{I}(^2P_{3/2})$  fragments.

## B. Theoretical results

### 1. 4D wavepacket calculations

The theoretical appearance times,  $\tau$ , for the  $\text{I}(^2P_{3/2})$  and  $\text{I}^*(^2P_{1/2})$  dissociation channels, the differences between appearance times,  $\Delta\tau$ , and the  $\text{I}/\text{I}^*$  branching ratios obtained with the 4D wavepacket method are collected in Table II and depicted in the top panel of Fig. 8 for the excitation wavelengths 243 nm and 268 nm.

For both wavelengths, the times associated with the  $\text{I}(^2P_{3/2})$  and  $\text{I}^*(^2P_{1/2})$  channels increase monotonically and smoothly with increasing vibrational excitation of the methyl fragment. The longer appearance times obtained for the reaction yielding vibrationally excited  $\nu_1 = 1$  methyl agree with the experimental results. However, the monotonic increase in the wavepacket appearance times  $\tau$  when  $\nu_2$  excitation in methyl increases is in contradiction with the non-monotonic behavior observed experimentally (see Fig. 7), as it was also found previously.<sup>15,16</sup>

The trend of the reaction times found theoretically is consistent with a monotonous and slight decrease in the energy available to the dissociation fragments as excitation in the vibrational modes of the  $\text{CH}_3$  fragment increases. Indeed, the appearance time increase is found to be rather small for excitation from  $\nu_2 = 0$  to  $\nu_2 = 2$  for the  $\text{I}$  and  $\text{I}^*$  channels correlated with either  $\text{CH}_3(\nu_1 = 0)$  or  $\text{CH}_3(\nu_1 = 1)$

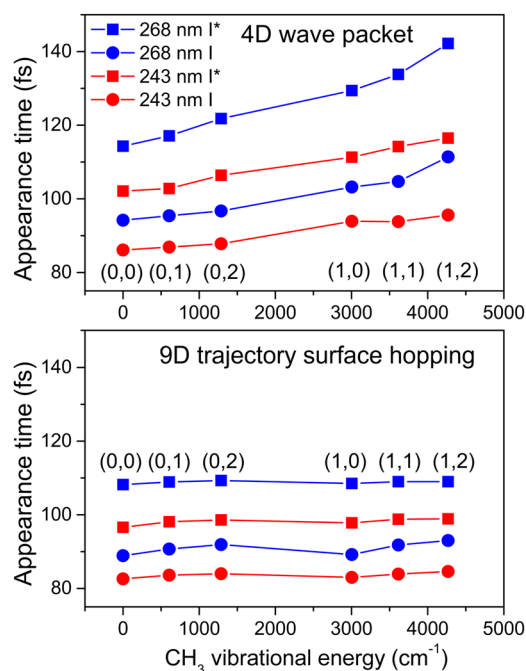


**FIG. 8.** Theoretical appearance times for the different  $\text{CH}_3(\nu_1, \nu_2) + \text{I}/\text{I}^*$  channels of the photodissociation of  $\text{CH}_3\text{I}$  at 243 nm (red symbols) and 268 nm (blue symbols) as a function of the excess vibrational energy of the  $\text{CH}_3$  fragment. Top: 4D wavepacket calculations. Bottom: 9D surface hopping trajectory calculations. Values in parentheses represent  $(\nu_1, \nu_2)$  vibrational quantum numbers.

because these  $\nu_2$  excitations involve a slight decrease in the energy available to the fragments. Excitation of the  $\nu_1$  mode from  $\nu_1 = 0$  to  $\nu_1 = 1$  implies a somewhat larger decrease in the available energy, which is reflected in a more significant increase in the reaction times of Table II.

The longer appearance times obtained when the available energy decreases due to larger vibrational excitation of the  $\text{CH}_3$  fragment is supported by the result found in Table II that the appearance

**TABLE II.** 4D wavepacket calculated appearance times  $\tau$  (in fs), differences between appearance times  $\Delta\tau$ , and  $\text{I}/\text{I}^*$  branching ratios measured for the different channels of the A-band photodissociation of  $\text{CH}_3\text{I}$  at the excitation wavelengths  $\lambda_{\text{exc}} = 268$  nm and 243 nm.

$\text{CH}_3(\nu_1, \nu_2)$	(0, 0)	(1, 0)	(0, 1)	(1, 1)	(0, 2)	(1, 2)
$\lambda_{\text{exc}} = 268$ nm						
$\text{I}(^2P_{3/2}), \tau$ (fs)	94.2	103.2	95.4	104.7	96.7	111.4
$\text{I}^*(^2P_{1/2}), \tau$ (fs)	114.3	129.4	117.1	133.8	121.8	142.2
$\Delta\tau$ (fs)	20.1	26.2	21.7	29.1	25.1	30.8
$\text{I}/\text{I}^*$ ratio	0.06	0.03	2.01	1.41	125.61	21.92
$\lambda_{\text{exc}} = 243$ nm						
$\text{I}(^2P_{3/2}), \tau$ (fs)	86.1	93.9	86.9	93.8	87.8	95.6
$\text{I}^*(^2P_{1/2}), \tau$ (fs)	102.1	111.3	102.8	114.2	106.4	116.5
$\Delta\tau$ (fs)	16.0	17.4	15.9	20.4	18.6	20.9
$\text{I}/\text{I}^*$ ratio	0.17	0.02	1.71	4.13	48.48	13.36

time increases slightly with increasing vibrational excitation for  $\lambda_{exc} = 243$  nm than for  $\lambda_{exc} = 268$  nm. The reason is that the energy difference between vibrational levels is constant for the two wavelengths and its contribution (in percentage) to the decrease in the total amount of available energy is smaller as the excitation wavelength becomes shorter (from 268 to 243 nm), leading to a lower time increase.

The variation of the time difference  $\Delta\tau$  between the I and I\* channels with vibrational excitation of the  $\nu_1$  and  $\nu_2$  modes follows the same trend for both excitation wavelengths. Similar arguments as the ones given above based on the amount of energy available to the fragments are applicable here. Indeed, similarly as with the appearance times  $\tau$ , variation of  $\Delta\tau$  is also smaller for  $\lambda_{exc} = 243$  nm than for  $\lambda_{exc} = 268$  nm. In addition, the  $\Delta\tau$  values are somewhat lower in the case of  $\lambda_{exc} = 243$  nm. Since the constant energy difference in the available energy to the fragments due to the spin-orbit splitting between the I and I\* channels is what originates  $\Delta\tau$ , again its relative contribution to the total available energy is smaller for the shorter wavelength, and thus, its effect on  $\Delta\tau$  becomes correspondingly smaller.

The I/I\* branching ratios also display the same behavior with vibrational excitation of the CH<sub>3</sub> fragment for the two excitation wavelengths. The trend shown is that the ratio increases with increasing excitation in the umbrella mode, indicating that a higher vibrational excitation in that mode is produced through the I dissociation channel compared to the I\* one. The same trend is found in

the experimental results of Table I, although the values of the theoretical ratios are, in general, quite different from the experimental ones. On the contrary, the theoretical I/I\* ratio decreases, in general, upon excitation from  $\nu = 0$  to  $\nu_1 = 1$  for the two excitation wavelengths.

Figure 9 displays the umbrella mode  $\nu_2$  vibrational distributions for the channels with CH<sub>3</sub> in  $\nu_1 = 0$  and  $\nu_1 = 1$  and I and I\* at the two excitation wavelengths 243 nm and 268 nm. As in previous works,<sup>15,16,56,57</sup> the vibrational distributions for the I\* channels are rather cold peaking at  $\nu_2 = 0$ , irrespective of the excitation wavelength. However, vibrational population inversion is observed for the I channels, the distributions peaking at  $\nu_2 = 1$  or 2. These observations are in good agreement with the existing experimental data.<sup>57</sup>

In summary, the present 4D wavepacket calculations carried out using the potential energy surfaces of Xie *et al.*<sup>24</sup> and the previously reported transition dipole moments,<sup>12</sup> in which a long enough C–I distance has been considered for the calculation of the state-resolved (both vibrational and electronic) appearance times such that the interaction between the iodine and methyl fragments is negligible (13 bohrs; 6.88 Å), demonstrate the minor role of the  $^3Q_0/{}^1Q_1$  conical intersection to influence the reaction times. Moreover, the small and monotonous trends observed in the theoretical appearance times as a function of vibrational excitation of the methyl fragment can be explained exclusively in terms of arguments based on the slightly different available energy in each case. Therefore, the observed nonmonotonous trend of the appearance times as a function of the vibrational energy content of the methyl fragment cannot be explained in terms of passing through the conical intersection between the  $^3Q_0$  and  ${}^1Q_1$  states.

## 2. 9D surface-hopping trajectory calculations

The theoretical appearance times,  $\tau$ , for the I( $^2P_{3/2}$ ) and I\*( $^2P_{1/2}$ ) dissociation channels, the differences between appearance times,  $\Delta\tau$ , and the I/I\* branching ratios obtained with the 9D (full dimension) surface-hopping trajectory method on the potential energy surfaces by Xie *et al.*<sup>24</sup> and the transition dipole moments of Ref. 12 are summarized in Table III and depicted in Fig. 8 for the excitation wavelengths 243 nm and 268 nm.

It is apparent from the semiclassical appearance times shown in the bottom panel of Fig. 8 and in Table III that at both excitation wavelengths, the times associated with the I( $^2P_{3/2}$ ) and I\*( $^2P_{1/2}$ ) channels increase monotonically and smoothly with increasing vibrational excitation of the methyl fragment, as it was the case in the 4D wavepacket calculations. In the present case, however, the increase is milder and, overall, the appearance times are always smaller (by about 7%–8%) than those obtained in the 4D wavepacket calculations, despite using the same final C–I distance to calculate the reaction times. There must be at least one explanation for this trend, which should be related with the different dimensionality of the two models; the fact that the semiclassical calculations are full dimension (9D) implies a larger randomization of the available energy into all the vibrational modes of the CH<sub>3</sub> fragment, and thus, the effect of the available energy in each case is milder. This monotonous and smooth dependence of the surface hopping trajectory appearance times as the vibrational energy content of the methyl fragment increases is, also in this case, at variance with the experimental observations. Despite the difference in

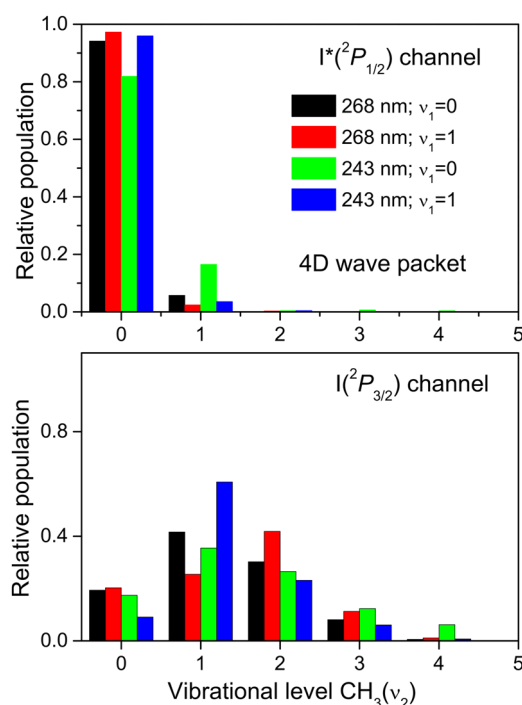


**FIG. 9.** Calculated vibrational distributions of the CH<sub>3</sub>( $\nu_2$ ) fragments produced in the photodissociation of CH<sub>3</sub>I at the excitation wavelengths 268 nm and 243 nm through the I\* channel (upper panel) and the I channel (lower panel) using the 4D wavepacket model.



**TABLE III.** 9D surface hopping trajectory appearance times  $\tau$  (in fs), differences between appearance times  $\Delta\tau$ , and  $I/I^*$  branching ratios measured for the different channels of the A-band photodissociation of  $\text{CH}_3\text{I}$  at the excitation wavelengths  $\lambda_{\text{exc}}$  268 nm and 243 nm.

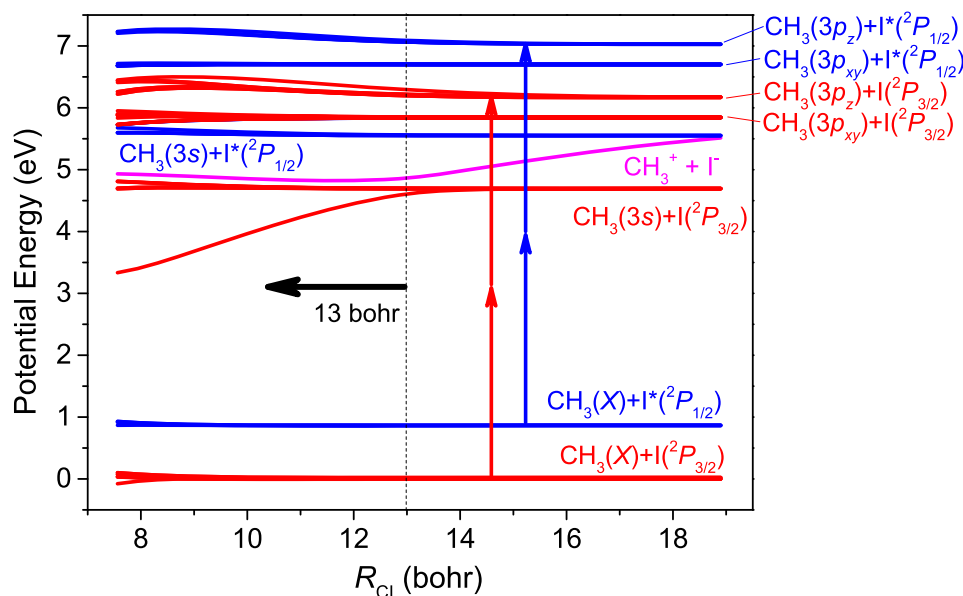
$\text{CH}_3(\nu_1, \nu_2)$	(0, 0)	(1, 0)	(0, 1)	(1, 1)	(0, 2)	(1, 2)
$\lambda_{\text{exc}} = 268 \text{ nm}$						
$\text{I}(^2P_{3/2}), \tau \text{ (fs)}$	88.9	89.2	90.7	91.8	91.9	93.0
$\text{I}^*(^2P_{1/2}), \tau \text{ (fs)}$	108.2	108.5	108.9	109.0	109.3	109.0
$\Delta\tau \text{ (fs)}$	19.5	19.3	18.2	17.2	17.4	16.0
$I/I^* \text{ ratio}$	0.09	0.09	0.28	0.42	0.57	1.00
$\lambda_{\text{exc}} = 243 \text{ nm}$						
$\text{I}(^2P_{3/2}), \tau \text{ (fs)}$	82.6	83.0	83.6	83.9	84.0	84.6
$\text{I}^*(^2P_{1/2}), \tau \text{ (fs)}$	96.6	97.8	98.1	98.8	98.6	98.9
$\Delta\tau \text{ (fs)}$	14.0	14.8	14.5	14.9	14.6	14.2
$I/I^* \text{ ratio}$	1.01	0.79	1.65	1.46	1.95	1.79

the dimensionality, the overall agreement between the appearance times calculated with the 4D wavepacket and 9D trajectory surface-hopping approaches is quite good, confirming that the degrees of freedom neglected in the quantum simulations are not really determinant to describe the photodissociation dynamics. We then conclude that the role of the conical intersection is minor, even when considering a full dimension calculation as in the present case.

The other observables,  $\Delta\tau$ ,  $I/I^*$  branching ratios, and the umbrella mode  $\nu_2$  vibrational distributions for the channels with  $\text{CH}_3$  in  $\nu_1 = 0$  and  $\nu_1 = 1$  and  $\text{I}$  and  $\text{I}^*$  (not shown), at the two excitation wavelengths 243 nm and 268 nm, follow similar trends as those observed in the 4D wavepacket calculations, and they will not be further discussed here.

### 3. *Ab initio* potential energy of the Rydberg states of $\text{CH}_3$

The clocking of the photodissociation of  $\text{CH}_3\text{I}$  after excitation at 268 nm and 243 nm studied in this work is carried out by probing the free  $\text{CH}_3$  fragment by resonance enhanced multiphoton ionization (REMPI) in a  $(2 + 1)$  process. This means that 2 photons of the same color, for instance, 333.5 nm for the REMPI process of vibrationless  $\text{CH}_3(\nu = 0)$ , are absorbed simultaneously from the vibrational ground state of the electronic ground state of  $\text{CH}_3$  to the  $3p_z$  Rydberg electronically excited state in its vibrational ground state ( $0_0^0$  transition in the REMPI spectrum). The third photon of the same color is then absorbed from that vibrational state of the Rydberg state to the ionization continuum, providing the  $\text{CH}_3^+$  that is

**FIG. 10.** Potential energy as a function of the C-I distance for the different electronic states of the  $\text{CH}_3$  radical, including the electronic ground state, the 3s,  $3p_{xy}$  and the  $3p_z$  Rydberg states, in correlation with  $\text{I}$  and  $\text{I}^*$ , and the ion-pair  $\text{I}^-\text{CH}_3^+$  state, calculated at the *ab initio* level described in Sec. II D. The vertical dashed line represents the C-I distance below of which the potential energy of the Rydberg states start to change (increase) as the iodine atom is approaching to the  $\text{CH}_3$  fragment. This is the C-I distance (13 bohrs) chosen in the theoretical treatments to calculate the appearance times. The double arrows (red and blue) represent the initial two-photon absorption for the  $(2 + 1)$  REMPI process employed for fragment detection.

detected. In order to clock the reaction, the resonant condition must be fulfilled, i.e., for the spectroscopic transition to occur, the  $\text{CH}_3$  radical has to be considered free of any measurable interaction with respect to the departing iodine atom, both in the ground electronic  $^2P_{3/2}$  and spin-orbit excited  $^2P_{1/2}$  states. In addition, the substantial bandwidth of the femtosecond laser probing pulse (about 2 nm) has to be considered to know when the pure spectroscopic transition occurs. The question would be then at what precise distance between the iodine and the methyl fragments, the resonant condition will be fulfilled.

To answer this question, we have carried out high level *ab initio* calculations of the potential energy dependence of the Rydberg states of  $\text{CH}_3$  on the C–I distance of the dissociating  $\text{CH}_3\text{I}$  molecule. Figure 10 depicts the potential energy of the different electronic states of the  $\text{CH}_3$  radical as a function of the C–I distance, considering the two asymptotes in each case, i.e., in correlation with I and  $\text{I}^*$ . The Rydberg states calculated for  $\text{CH}_3$  are the  $3s$ , the degenerate  $3p_x$  and  $3p_y$  and the  $3p_z$ , which are the lowest lying electronic excited states. In addition, the ion-pair  $\text{I}^+\text{CH}_3^+$  state appears and interacts with the  $3s$  state at about 7 Å. A close inspection of the potential energy curves indicates that at shorter C–I distances than about 13 bohrs (6.88 Å), the Rydberg states start to distort (increasing in energy), and in some cases, they split into different curves. Indeed, this is the C–I distance we have chosen to calculate the appearance times using both theoretical methods (see above).

In addition to the potential energy curves, we have calculated the corresponding adiabatic potential energy curves (adiabats) for the umbrella mode  $\nu_2$  vibrational states of  $\text{CH}_3$ . One possible explanation for the nonmonotonous trend in the observed clocking times (see Fig. 7) could be that the C–I distance, where the distortion of the potential energy starts, given the proximity of the heavy iodine atom, would be different for the different  $\nu_2$  vibrational states of  $\text{CH}_3$ , and thus, each pure vibronic transition ( $0_0^0$ ,  $1_1^1$ ,  $2_1^1$ , and  $2_2^2$ ) providing the clocking of each channel would occur at a slightly different C–I distance. Figure 11 depicts the potential energy

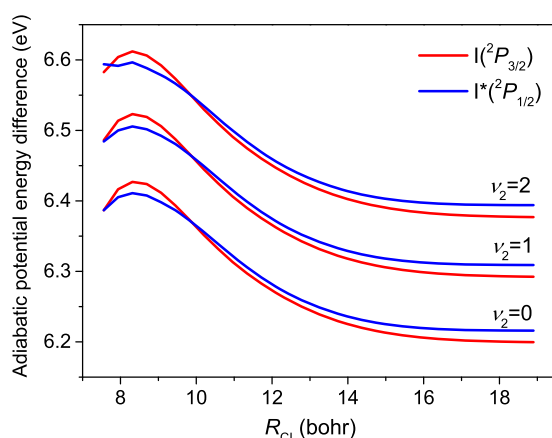


**FIG. 11.** Differences between the ground state and  $3p_z$  Rydberg adiabatic potential energy curves of  $\text{CH}_3$  as a function of the C–I distance, calculated at the *ab initio* level described in Sec. II D.

difference between the adiabats of the electronic ground state of  $\text{CH}_3$  and those of the  $3p_z$  Rydberg state, which are involved in the (2 + 1) REMPI process used for the detection of the different vibrational states of the free  $\text{CH}_3$ . As can be seen, all the differences between the adiabat curves are rather similar and parallel, and thus, the vibronic transitions involved in the clocking of the different vibrational states of  $\text{CH}_3$  would occur at approximately the same C–I distance of the photodissociating molecule. The conclusion is that the probing step would not explain the nonmonotonous appearance times measured for the different vibrational states of the  $\text{CH}_3$  fragment.

#### IV. DISCUSSION

One of the issues that has provoked controversy around the photodissociation of  $\text{CH}_3\text{I}$  in the A-band is the relative contribution to absorption to different excited states across the band. It is well established that in the center of the band at around 260 nm, absorption to the  $^3Q_0$  state is predominant, leading adiabatically to the formation of spin-orbit excited  $\text{I}^*(^2P_{1/2})$ . Since the strength of absorption to the  $^1Q_1$  state is very low, the observed ground state iodine  $\text{I}(^2P_{3/2})$  must originate mostly nonadiabatically from the existing  $^3Q_0/{}^1Q_1$  conical intersection. The issue was addressed in previous experimental work,<sup>13</sup> which concluded that the participation of the  $^1Q_1$  state is dominant only at the blue edge of the absorption band at 217 nm but very significantly reduced already at 230 nm, as it is also deduced from the  $\beta_2$  anisotropy parameters depicted in Fig. 3. For the absorption examined in this work at the blue side of the absorption band at 243 nm, the strong parallel character observed in the methyl images correlating with both  $\text{I}/\text{I}^*$  channels and the large values of the  $\beta_2$  anisotropy parameter close to the maximum of 2 for a parallel transition constitutes further indication of the minor role played by the  $^1Q_1$  state at this excitation wavelength. However, we have observed longer reaction times at  $\lambda_{\text{exc}} = 243$  nm when excitation to the umbrella mode of  $\text{CH}_3$  is produced in comparison with vibrationless  $\text{CH}_3$  for both  $\nu_1 = 0$  and  $\nu_1 = 1$  and for both electronic channels yielding I and  $\text{I}^*$  (see Table and Figure). This trend is surprising and unexpected when compared to the results obtained at  $\lambda_{\text{exc}} = 268$  nm and cannot be attributed to the probing step, which is exactly the same for the experiments carried out at the two excitation wavelengths.

Interestingly, Warne *et al.*<sup>33</sup> recently reported experiments carried out at 269 nm and 255 nm using a 2-photon ionization probe at 395 nm in time-resolved photoelectron imaging, in which they observe different dynamics at the two excitation wavelengths with significant changes in the lifetimes and dynamic structure. The lifetime measured for the departure of the initial wavepacket out of the ionization Franck-Condon region after excitation at 268 nm was found to be 30 fs, which would be consistent with measurements of the formation of products carried out in this work. However, after excitation at 255 nm, although a similar process is observed in a first decay component, a secondary feature associated with a delayed component by about 100 fs is found. The authors of Ref. 33 suggest that this delayed feature is due to excited state population and specific dynamics on the  $^1Q_1$  potential energy surface, undergoing significant rearrangement prior to dissociation. This explanation is, however, not very plausible in

view of the 4D wavepacket, and 9D surface-hopping trajectory calculations carried out in this work, which demonstrate that an absorption spectrum where the contribution of the  $^1Q_1$  state is overestimated, cannot explain a distinct dynamics occurring in this state (see, for instance, Fig. 8). It may happen that the accidental resonance in the probing step, where resonance enhanced ionization through the  $6p$  Rydberg state occurs, can explain the distinct features found at this excitation wavelength. More experiments of the same class but carried out at different probing wavelengths to avoid any accidental resonance may help us to understand the observed features.

Once the role of the absorption to the  $^1Q_1$  state or the  $^3Q_0/{}^1Q_1$  conical intersection can be disregarded as a cause of the characteristic appearance times observed as a function of the final umbrella vibrational quantum state of  $\text{CH}_3$  at the two excitation wavelengths studied in this work (268 and 243 nm), we have to rely again on the  $(2 + 1)$  REMPI probing step through the  $3p_z$  Rydberg state of  $\text{CH}_3$  to try to explain the observations. We have demonstrated in Sec. III B 3 that *ab initio* calculations of the adiabatic potential energy curves (as a function of the C–I distance) cannot explain that the optical window determined by the bandwidth of the probe laser pulse accessed by two-photon absorption is open at different C–I distances for the different umbrella vibrational states of  $\text{CH}_3$  (see Figs. 10 and 11), which might explain the experimental results. However, it may happen that the efficiency of the two-photon absorption at the specific wavelengths for the  $0_0^0$ ,  $2_1^1$ , and  $2_2^2$  transitions in  $\text{CH}_3$  depends on the final vibrational state of the  $3p_z$  Rydberg state. It is well known that the  $3p_z$  Rydberg state of  $\text{CH}_3$  is predissociative due to the presence of valence states.<sup>58–60</sup> The predissociation rate depends on the vibrational state accessed in the  $3p_z$  Rydberg state of the fragment, being faster as vibrational excitation increases.<sup>58</sup> Actually, REMPI spectroscopy of  $\text{CH}_3$  is limited by the extension of this predissociation, which precludes the detection of highly excited vibrationally states. We do not know the effect of the presence of the heavy iodine atom on the valence states and on the predissociation rate, but if higher vibrational states of the Rydberg would be more affected by the presence of the iodine atom, then unexpected effects on the probing process could arise, affecting the appearance times in an undetermined way. Clocking experiments on the isotopic variant  $\text{CD}_3\text{I}$  would be very timely as predissociation is less effective in deuterated methyl ( $\text{CD}_3$ ). Moreover, given that the Franck-Condon region accessed by excitation at 243 nm is somewhat different than that at 268 nm excitation, the combination of the 243 nm pump and  $(2 + 1)$  REMPI detection of the  $\text{CH}_3$  fragment can yield different dependences on the clocking times of the umbrella vibrational mode excitation than at 268 nm.

Unfortunately, none of the probe spectroscopies used recently to study the time-resolved photodissociation of  $\text{CH}_3\text{I}$  in the A-band, which includes two-photon ionization photoelectron spectroscopy, soft X-ray inner-shell photoelectron spectroscopy, VUV single-photon ionization, and XUV core-to-valence transient absorption spectroscopy, have been able to measure vibrationally state-resolved lifetimes or appearance times. The use of other laser spectroscopic techniques for the detection of quantum state-resolved  $\text{CH}_3$  without the limitations of REMPI would be very timely to confirm or disregard the vibrational state effects on the clocking times.

## V. CONCLUSIONS

A critical report on the clocking of the chemical bond cleavage at the heart of Femtochemistry has been presented by experimentally and theoretically studying the photodissociation of  $\text{CH}_3\text{I}$  upon absorption in the center (268 nm) and in the blue side (243 nm) of the A-band. The clocking of vibrationally and electronic state-resolved channels of the reaction is carried out by resonance enhanced multiphoton ionization of the  $\text{CH}_3$  fragment. In particular, vibrationless methyl and vibrationally excited to the  $\nu_2$  umbrella bending and  $\nu_1$  symmetric stretch modes have been detected by  $(2 + 1)$  REMPI through the intermediate  $3p_z$  Rydberg state. Distinct trends of the clocking times as a function of the vibrational excitation of  $\text{CH}_3$  are observed at both excitation wavelengths, which are at variance of theoretical calculations consisting in 4D wavepacket and 9D trajectory surface hopping carried out on the available full dimension *ab initio* potential energy surfaces and transition dipole moments for the ground and excited  $^3Q_0$  and  $^1Q_1$  states. The role of the  $^3Q_0/{}^1Q_1$  conical intersection or a significant absorption to the  $^1Q_1$  state have been discarded to explain the observed vibrationally state-resolved clocking times at the two excitation wavelengths. *Ab initio* calculations of the adiabatic ground and excited state potential energy curves of the  $\text{CH}_3$  radical as a function of the distance to the heavy iodine atom cannot account for specific opening of the optical window for different vibrational states of  $\text{CH}_3$ . However, the nonadiabatic coupling between valence states and the  $3p_z$  Rydberg state of the  $\text{CH}_3$  fragment gives rise to efficient electronic predissociation whose rate increases with the vibrational excitation. The presence of the heavy iodine atom may affect differently the couplings and predissociation rate of the different vibrational states of  $\text{CH}_3$ , and this would have unpredictable effects on the clocking times measured. More experiments using deuterated  $\text{CD}_3\text{I}$ , where  $\text{CD}_3$  predissociation is much less efficient, and/or the use of a different laser spectroscopy technique, which allows the detection of quantum state-resolved products, would be important to finally disentangle the effect of internal degrees of freedom of the molecular fragment in the clocking of state-resolved channels in the photodissociation of  $\text{CH}_3\text{I}$ .

## ACKNOWLEDGMENTS

M.L.M.-S. acknowledges financial support through a predoctoral contract from Universidad Complutense de Madrid. M.E.C. is grateful to the Spanish MINECO for a contract through Programa de Técnicos de Apoyo a Infraestructuras. This work was financially supported by the Spanish MINECO and MICIU (Grant Nos. CTQ2016-75880-P, FIS2016-77889-R, and PGC2018-096444-B-I00). This research was carried out within the Unidad Asociada Química Física Molecular between the Departamento de Química Física of Universidad Complutense de Madrid and CSIC. The facilities provided by the Center for Ultrafast Lasers of Universidad Complutense de Madrid are acknowledged.

## REFERENCES

- 1 M. J. Rosker, M. Dantus, and A. H. Zewail, *J. Chem. Phys.* **89**, 6113 (1988).
- 2 A. H. Zewail, *Science* **242**, 1645 (1988).
- 3 A. H. Zewail, *Angew. Chem., Int. Ed.* **39**, 2586 (2000).

- <sup>4</sup>M. Dantus, M. J. Rosker, and A. H. Zewail, *J. Chem. Phys.* **89**, 6128 (1988).
- <sup>5</sup>T. S. Rose, M. J. Rosker, and A. H. Zewail, *J. Chem. Phys.* **91**, 7415 (1989).
- <sup>6</sup>A. H. Zewail, *J. Phys. Chem. A* **102**, 4031 (1998).
- <sup>7</sup>A. Gedanken and M. D. Rowe, *Chem. Phys. Lett.* **34**, 39 (1975).
- <sup>8</sup>Y. Amatatsu, S. Yabushita, and K. Morokuma, *J. Chem. Phys.* **104**, 9783 (1996).
- <sup>9</sup>D. W. Chandler and P. L. Houston, *J. Chem. Phys.* **87**, 1445 (1987).
- <sup>10</sup>A. T. J. B. Eppink and D. H. Parker, *J. Chem. Phys.* **109**, 4758 (1998).
- <sup>11</sup>A. T. J. B. Eppink and D. H. Parker, *J. Chem. Phys.* **110**, 832 (1999).
- <sup>12</sup>L. Rubio-Lago, A. García-Vela, A. Arregui, G. A. Amaral, and L. Bañares, *J. Chem. Phys.* **131**, 174309 (2009).
- <sup>13</sup>M. G. González, J. Rodríguez, L. Rubio-Lago, A. García-Vela, A. Arregui, G. A. Amaral, and L. Bañares, *Phys. Chem. Chem. Phys.* **13**, 16404 (2011).
- <sup>14</sup>R. de Nalda, J. G. Izquierdo, J. Durá, and L. Bañares, *J. Chem. Phys.* **126**, 021101 (2007).
- <sup>15</sup>R. de Nalda, J. Durá, A. García-Vela, J. G. Izquierdo, J. González-Vázquez, and L. Bañares, *J. Chem. Phys.* **128**, 244309 (2008).
- <sup>16</sup>A. García-Vela, R. de Nalda, J. Durá, J. González-Vázquez, and L. Bañares, *J. Chem. Phys.* **135**, 154306 (2011).
- <sup>17</sup>M. E. Corrales, V. Lorient, G. Balerdi, J. González-Vázquez, R. de Nalda, L. Bañares, and A. H. Zewail, *Phys. Chem. Chem. Phys.* **16**, 8812 (2014).
- <sup>18</sup>J. Durá, R. de Nalda, J. Álvarez, J. G. Izquierdo, G. A. Amaral, and L. Bañares, *ChemPhysChem* **9**, 1245 (2008).
- <sup>19</sup>J. Durá, R. de Nalda, G. A. Amaral, and L. Bañares, *J. Chem. Phys.* **131**, 134311 (2009).
- <sup>20</sup>Y. Amatatsu, K. Morokuma, and S. Yabushita, *J. Chem. Phys.* **94**, 4858 (1991).
- <sup>21</sup>H. Guo and G. C. Schatz, *J. Chem. Phys.* **93**, 393 (1990).
- <sup>22</sup>H. Guo, *J. Chem. Phys.* **96**, 6629 (1992).
- <sup>23</sup>A. D. Hammerich, U. Manthe, R. Kosloff, H.-D. Meyer, and L. S. Cederbaum, *J. Chem. Phys.* **101**, 5623 (1994).
- <sup>24</sup>D. Q. Xie, H. Guo, Y. Amatatsu, and R. Kosloff, *J. Phys. Chem. A* **104**, 1009 (2000).
- <sup>25</sup>A. B. Alekseyev, H. Liebermann, R. J. Buenker, and S. N. Yurchenko, *J. Chem. Phys.* **126**, 234102 (2007).
- <sup>26</sup>A. B. Alekseyev, H. Liebermann, and R. J. Buenker, *J. Chem. Phys.* **126**, 234103 (2007).
- <sup>27</sup>C. R. Evenhuis and U. Manthe, *J. Phys. Chem. A* **115**, 5992 (2011).
- <sup>28</sup>N. Wittenbrink and W. Eisfeld, *J. Chem. Phys.* **148**, 094102 (2018).
- <sup>29</sup>A. R. Attar, A. Bhattacharjee, and S. R. Leone, *J. Phys. Chem. Lett.* **6**, 5072 (2015).
- <sup>30</sup>L. Drescher, M. C. E. Galbraith, G. Reitsma, J. Durá, N. Zhavoronkov, S. Patchkovskii, M. J. J. Vrakking, and J. Mikosch, *J. Chem. Phys.* **145**, 011101 (2016).
- <sup>31</sup>A. Baumann, D. Rompotis, O. Schepp, and M. Wieland, *J. Phys. Chem. A* **122**, 4779 (2018).
- <sup>32</sup>F. Brauße, G. Goldsztejn, K. Amini, R. Boll, S. Bari, C. Bomme, M. Brouard, M. Burt, B. C. de Miranda, S. Düsterer *et al.*, *Phys. Rev. A* **97**, 043429 (2018).
- <sup>33</sup>E. M. Warne, B. Downes-Ward, J. Woodhouse, M. A. Parkes, D. Bellshaw, E. Springate, P. Majchrzak, Y. Zhang, G. Karras, A. S. Wyatt *et al.*, *Phys. Chem. Chem. Phys.* **21**, 11142 (2019).
- <sup>34</sup>A. T. Eppink and D. H. Parker, *Rev. Sci. Instrum.* **68**, 3477 (1997).
- <sup>35</sup>G. A. Garcia, L. Nahon, and I. Powis, *Rev. Sci. Instrum.* **75**, 4989 (2004).
- <sup>36</sup>V. Lorient, R. de Nalda, and L. Bañares, *Appl. Sci.* **8**, 1227 (2018).
- <sup>37</sup>W. Arbelo-González, L. Bonnet, and A. García-Vela, *Phys. Chem. Chem. Phys.* **15**, 9994 (2013).
- <sup>38</sup>W. Arbelo-González, L. Bonnet, and A. García-Vela, *J. Chem. Phys.* **142**, 134111 (2015).
- <sup>39</sup>M. Richter, P. Marquetand, J. González-Vázquez, I. Solá, and L. González, *J. Chem. Theory Comput.* **7**, 1253 (2011).
- <sup>40</sup>H.-J. Werner, P. J. Knowles, R. Lindh, F. R. Manby, M. Schütz, P. Celani, T. Korona, A. Mitrushenkov, G. Rauhut, T. B. Adler *et al.*, *MOLPRO*, version 2012.1, a package of *ab initio* programs, 2012, see <http://www.molpro.net>.
- <sup>41</sup>J. Petersen and R. Mitrić, *Phys. Chem. Chem. Phys.* **14**, 8299 (2012).
- <sup>42</sup>J. C. Corchado and J. Espinosa-García, *Phys. Chem. Chem. Phys.* **11**, 10157 (2009).
- <sup>43</sup>C. W. Eaker and G. C. Schatz, *J. Chem. Phys.* **81**, 2394 (1984).
- <sup>44</sup>C. W. Eaker, G. C. Schatz, N. DeLeon, and E. J. Heller, *J. Chem. Phys.* **81**, 5913 (1984).
- <sup>45</sup>J. Binney and D. Spergel, *Mon. Not. R. Astron. Soc.* **206**, 159 (1964).
- <sup>46</sup>C. C. Martens and G. S. Ezra, *J. Chem. Phys.* **83**, 2990 (1985).
- <sup>47</sup>L. J. Curtis and D. G. Ellis, *Am. J. Phys.* **72**, 1521 (2004).
- <sup>48</sup>S. A. Vázquez and E. Martínez-Núñez, *Phys. Chem. Chem. Phys.* **17**, 6948 (2015).
- <sup>49</sup>M. J. Wilhelm, E. Martínez-Núñez, J. González-Vázquez, S. A. Vázquez, J. M. Smith, and H.-L. Dai, *Astrophys. J.* **15**, 849 (2017).
- <sup>50</sup>B. O. Roos, R. Lindh, P.-A. Malmqvist, V. Veryazov, and P.-O. Widmark, *J. Phys. Chem. A* **108**, 2851 (2004).
- <sup>51</sup>M. Reiher and A. Wolf, *J. Chem. Phys.* **121**, 10945 (2004).
- <sup>52</sup>B. Schimmelpennig, *Amfi, an atomic mean-field spin-orbit integral program* (Stockholm University, 1996).
- <sup>53</sup>I. Fernández Galván, M. Vacher, A. Alavi, C. Angeli, F. Aquilante, J. Autschbach, J. J. Bao, S. I. Bokarev, N. A. Bogdanov, R. K. Carlson *et al.*, *J. Chem. Theory Comput.* **15**, 5925–5964 (2019).
- <sup>54</sup>C. C. Martson and G. G. Balint-Kurti, *J. Chem. Phys.* **91**, 3571 (1989).
- <sup>55</sup>G. Gitzinger, M. E. Corrales, V. Lorient, R. de Nalda, and L. Bañares, *J. Chem. Phys.* **136**, 074303 (2012).
- <sup>56</sup>A. García-Vela and L. Bañares, *Phys. Chem. Chem. Phys.* **13**, 2228 (2011).
- <sup>57</sup>A. García-Vela and L. Bañares, *Eur. Phys. J. D* **67**, 265 (2013).
- <sup>58</sup>G. Balerdi, J. Woodhouse, A. Zanchet, R. de Nalda, M. L. Senent, A. García-Vela, and L. Bañares, *Phys. Chem. Chem. Phys.* **18**, 110 (2016).
- <sup>59</sup>S. Marggi Poullain, D. V. Chicharro, A. Zanchet, M. G. González, L. Rubio-Lago, M. L. Senent, A. García-Vela, and L. Bañares, *Phys. Chem. Chem. Phys.* **18**, 17054 (2016).
- <sup>60</sup>A. Zanchet, L. Bañares, M. L. Senent, and A. García-Vela, *Phys. Chem. Chem. Phys.* **18**, 33195 (2016).